

# Inflow velocities of cold flows streaming into massive galaxies at high redshifts

Tobias Goerdt<sup>1\*</sup> and Daniel Ceverino<sup>2</sup>

<sup>1</sup>*Institut für Astrophysik, Türkenschanzstraße 17, Universität Wien, 1180 Wien, Österreich*

<sup>2</sup>*Centro de Astrobiología (CSIC-INTA), Ctra de Torrejón a Ajalvir, km 4, 28850 Torrejón de Ardoz, Madrid, España*

Draft version 22 November 2021

## ABSTRACT

We study the velocities of the accretion along streams from the cosmic web into massive galaxies at high redshift with the help of three different suites of AMR hydrodynamical cosmological simulations. The results are compared to free-fall velocities and to the sound speeds of the hot ambient medium. The sound speed of the hot ambient medium is calculated using two different methods to determine the medium’s temperature. We find that the simulated cold stream velocities are in violent disagreement with the corresponding free-fall profiles. The sound speed is a better albeit not always correct description of the cold flows’ velocity. Using these calculations as a first order approximation for the gas inflow velocities  $v_{\text{inflow}} = 0.9 v_{\text{vir}}$  is given. We conclude from the hydrodynamical simulations as our main result that the velocity profiles for the cold streams are constant with radius. These constant inflow velocities seem to have a “parabola-like” dependency on the host halo mass in units of the virial velocity that peaks at  $M_{\text{vir}} = 10^{12} M_{\odot}$  and we also propose that the best fit functional form for the dependency of the inflow velocity on the redshift is a square root power law relation:  $v_{\text{inflow}} \propto \sqrt{z+1} v_{\text{vir}}$ .

**Key words:** cosmology: theory – galaxies: evolution – galaxies: formation – galaxies: high redshift – intergalactic medium – methods: numerical

## 1 INTRODUCTION

In the recent years it has been shown in theoretical work and in simulations (Fardal et al. 2001; Birnboim & Dekel 2003; Kereš et al. 2005, 2009; Dekel & Birnboim 2006; Ocvirk, Pichon & Teyssier 2008; Dekel et al. 2009a, 2013) that massive galaxies in the high redshift regime ( $z \gtrsim 1.5$ ), acquire their baryons primarily via cold narrow streams of relatively dense and pristine gas with temperatures around  $10^4$  K. These cold flows penetrate through the diffuse shock-heated medium. Their activity peaks around redshift 3. Having reached the inner parts of the host halo their gas will eventually form a dense, unstable, turbulent disc with a bulge where rapid star formation is triggered (Agertz, Teyssier & Moore 2009, 2011; Dekel, Sari & Ceverino 2009b; Ceverino, Dekel & Bournaud 2010; Krumholz & Burkert 2010; Ceverino et al. 2012, 2014, 2015; Cacciato, Dekel & Genel 2012; Genel, Dekel & Cacciato 2012; Genzel et al. 2011; Mandelker et al. 2014).

Galaxies’ gas depletion time scales are understood to be short with respect to the Hubble time throughout cosmic history (Daddi et al. 2010; Genzel et al. 2010). So it becomes apparent that galaxies must accrete fresh gas from the intergalactic medium to sustain the observed levels of star formation over such a long time, since otherwise their gas reservoirs would have been completely emptied. In the cold flow scenario star formation behaves like a shower that is not draining properly: no matter what are the initial conditions, a steady state will be reached at the point where the amount of material that comes in via cold streams is equal to the drained material, i.e. the gas that is being lost by star formation and outflows. In the bathtub it is that the pressure at the bottom that rises as it gets more full, pushing out more water. For galaxies, it is the star formation rate that increases with the increase of available gas. The result is a self-regulated system, the accretion is driving the star-formation rate and not the amount of available gas (Bouché et al. 2010). It is in this sense that the star formation rate of a galaxy is fundamentally limited by its gas inflow and does not depend so much on local physics, such as how well the feedback regulates it. The timescales for star

\* tobias.goerdt@univie.ac.at

formation as well as the star formation rate both depend crucially on the gas accretion rate, which in turn depends on the speed of the infalling gas when it reaches the halo centre. So doubling the infall velocity would also result in doubling the star formation rate assuming constant cold stream cross sections and densities, which highlights the importance of the inflow velocity.

Processes of observing the cold accretion stream paradigm in the real universe are ongoing. Goerdt et al. (2012) made theoretical predictions about the likelihood of observing these streams in absorption. Striking features in absorption have indeed been observed (Bouché et al. 2013). Ibata et al. (2013) found the existence of a planar subgroup of satellites in the Andromeda galaxy (M 31), comprising about half the population. Goerdt, Burkert & Ceverino (2013) demonstrated that this vast thin disk of satellites can naturally be explained within the cold stream framework and should therefore be interpreted as indirect observational evidence for the cold stream paradigm.

Goerdt et al. (2010) used the cold stream model to explain the observational phenomenon of Ly $\alpha$ -blobs (LABs). They deployed cosmological hydrodynamical AMR simulations to predict the characteristics of Ly $\alpha$  emission from the cold gas streams. These authors pointed out that in their simulations the velocities of the cold streams are constant. So the potential energy of the inflowing gas is not converted into kinetic energy. Subsequently they concluded that it is the release of gravitational energy as the gas is flowing down the potential gradient towards the halo centre which powers the Ly $\alpha$  luminosity. The potential energy of the inflowing gas is released as Ly $\alpha$  radiation. This model was put forward as an alternative to other models trying to explain the emission of LABs like being produced in the galaxy's H II regions but then being scattered in our direction by the H I gas in the galaxy's circum-galactic medium (Steidel et al. 2011), being lit up due to illumination from a nearby buried AGN (Basu-Zych & Scharf 2004; Scarlata et al. 2009; Prescott et al. 2015) or being lit up due to stellar feedback (Chapman et al. 2001; Geach et al. 2005, 2007).

Faucher-Giguere et al. (2010) tested the results of Goerdt et al. (2010). They analysed cosmological smoothed particle hydrodynamics simulations to predict the Ly $\alpha$  cooling emission of forming galaxies with the help of a Ly $\alpha$  radiative transfer code. In contrast to Goerdt et al. (2010) they mention that a scenario in which the cold streams free-fall into the haloes and release little energy before hitting the central disk in a strong shock, may be supported by their results. Later also Rosdahl & Blaizot (2012) addressed the same question independently. For this purpose they ran and analysed cosmological radiation-hydrodynamics simulations. They looked at phase diagrams for their haloes of gas speed versus radius in which they were able to distinguish several cold streams. They produced corresponding free-fall profiles (i.e. the speeds that the streams would follow if they were in free-fall). In contrast to Goerdt et al. (2010) they concluded that the streams are close to free-fall. As we will also discuss in greater depth in section 5, the discrepancies between their work and the results presented later in this paper might result from the fact, that Faucher-Giguere et al. (2010) on the one hand deployed SPH simulations which used to have inaccuracies modelling dis-

sipative processes (Agertz et al. 2007) and the sample of galaxies of Rosdahl & Blaizot (2012) on the other hand was very small (only three galaxies in total) and they report that not all of their galaxies showed signs of free-fall behaviour.

Radial velocities around  $10^{12} M_{\odot}$  haloes have been studied (van de Voort & Schaye 2012). They found roughly constant values of the radial inflow velocities, with a decrease towards smaller radii.

Nelson et al. (2013) compare results from SPH with moving mesh simulations and find that the filamentary geometry of accreting gas near the virial radius is a common feature in massive haloes above  $10^{11.5} M_{\odot}$ . Gas filaments in GADGET, however, tend to remain collimated and flow coherently to small radii, or artificially fragment and form a large number of purely numerical blobs. These same filamentary gas streams in AREPO show increased heating and disruption at  $0.25 - 0.5 r_{\text{vir}}$  and contribute to the hot gas accretion rate in a manner distinct from classical cooling flows.

Nelson et al. (2015a) investigated how the way galaxies acquire their gas across cosmic time in cosmological hydrodynamic simulations is modified by a comprehensive physical model for baryonic feedback processes finding that feedback strongly suppresses the raw, as well as the net, inflow of this smooth mode gas at all redshifts, regardless of the temperature history of newly acquired gas.

Wetzel & Nagai (2014) explored systematically the physics that governs cosmic accretion into haloes and their galaxies. They analysed a suite of cosmological simulations that incorporate both dark matter and gas dynamics with differing treatments of gas cooling, star formation and thermal feedback to explore the physics that governs the accretion of dark matter and baryons into halos and their galaxies. They presented average radial velocities of the inflowing material (their figures 4 and 6, bottom panels). The inflow velocities presented there decrease with decreasing radius (roughly a decrease of 65% between  $1 r_{\text{vir}}$  and the centre of the host).

In a companion paper (Goerdt et al. 2015) we look at the amount of inflow – the mass accretion rate – both as a function of radius, mass and redshift for the three constituents gas, stars and dark matter.

In this paper we look at the velocity profiles of the gas inflow, both as a function of radius, mass and redshift for the three constituents of the simulations, namely gas, stars and dark matter. This study is worthwhile doing since multiphase gas accretion is an interesting topic in galaxy formation theory by itself and this study in particular has important implications on the judgement of plausibility of both star formation rates as well as the gravitational cooling model for LABs, as already mentioned. The paper is organised as follows: in section 2 we present the three suites of simulations used for the following analysis. In section 3 we show a brief analysis of the mass accretion rate of the gas. In section 4 we present our toy models. In section 5 we discuss the velocity profiles of the inflow along the streams and in section 6 we draw our conclusions.

## 2 SIMULATIONS

We use snapshots of galaxies from three different sets of simulations, all three employing Eulerian AMR (Adaptive Mesh

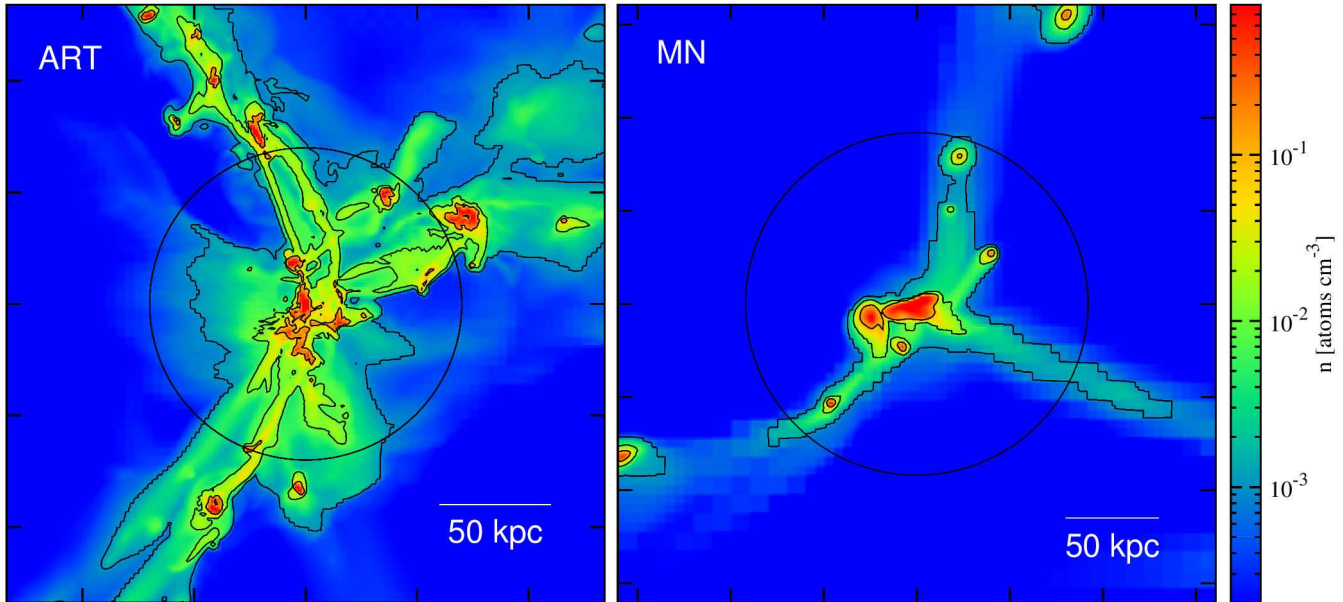


**Figure 1.** Two simulated galaxies from ART and MN. The colour refers to the maximum gas density along the line of sight. Contour lines are at  $n = 0.1, 0.01$  and  $0.001 \text{ cm}^{-3}$ , respectively. The circles show the virial radii. Left: a typical ART galaxy (resolution 70 pc) at  $z = 2.3$ , with  $M_{\text{vir}} = 3.5 \times 10^{11} M_{\odot}$ . Right: one of the MN galaxies (resolution 1 kpc) at  $z = 2.5$ , with  $M_{\text{vir}} = 10^{12} M_{\odot}$ . In both cases, the inflow is dominated by three cold narrow streams that are partly clumpy. The density in the streams is  $n = 0.003 - 0.1 \text{ cm}^{-3}$ , with the clump cores reaching  $n \sim 1 \text{ cm}^{-3}$ .

Refinement) hydrodynamics in a cosmological setting. The ART (Ceverino, Dekel & Bournaud 2010; Ceverino et al. 2012; Dekel et al. 2013; Ceverino et al. 2015) suite consists of several zoom-in simulations with a maximum resolution of 35 – 70 pc at  $z = 2$ . The simulation zooms in on individual galaxies that reside in dark-matter haloes which have masses of  $(0.13 - 1.60) \times 10^{12} M_{\odot}$  at  $z = 2.3$ . This ART suite has got an extension that we will also use, the  $A_{\text{RP}}$  suite of simulations which includes radiation pressure feedback (Ceverino et al. 2014). This second suites consist of individual galaxies that reside in dark-matter haloes of masses  $(1 - 8) \times 10^{11} M_{\odot}$  at  $z = 2.0$ . The third simulation is the Horizon-MareNostrum (hereafter MN) simulation (Ocvirk, Pichon & Teyssier 2008) containing dozens of massive galaxies in a cosmological box of side 71 Mpc with a maximum resolution of  $\leq 1 \text{ kpc}$ .

Density maps of galaxies of the MN as well as the ART suite are shown in figure 1. They demonstrate the dominance of typically three, narrow cold streams, which come from well outside the virial radius along the dark-matter filaments of the cosmic web, and penetrate into the discs at the halo centres. The streams are partly clumpy and partly smooth, even in the simulation of higher resolution. The typical densities in the streams are in the range  $n = 0.01 - 0.1 \text{ cm}^{-3}$ , and they reach  $n = 0.1 - 1 \text{ cm}^{-3}$  at the clump centres and in the central disk.

## 2.1 High-resolution ART simulations

These simulations were run with the AMR code ART (Adaptive Refinement Tree; Kravtsov, Klypin & Khokhlov 1997; Kravtsov 2003) with a spatial resolution better than 70 pc in physical units. It incorporates gas cooling, photoionisation

heating, star formation, metal enrichment and stellar feedback (Ceverino & Klypin 2009) which are relevant physical processes for galaxy formation. For the gas density, temperature, metallicity, and UV background in any given cell cooling rates were computed using CLOUDY (Ferland et al. 1998). It is assumed that cooling takes place at the centre of a cloud of thickness 1 kpc (Ceverino-Rodriguez 2008; Robertson & Kravtsov 2008). Metallicity dependent, metal-line cooling is also included, assuming a relative abundance of elements equal to the solar composition. The code implements a “constant” feedback model, in which the combined energy from stellar winds and supernova explosions is released as a constant heating rate over 40 Myr (the typical age of the lightest star that can still explode in a type-II supernova). Photo-heating is taken into account self-consistently with radiative cooling. A uniform UV background (Haardt & Madau 1996) is assumed, ignoring local sources. The self-shielding of dense, galactic neutral hydrogen from the cosmological UV background is mimicked by assuming a substantially suppressed UV background ( $5.9 \times 10^{26} \text{ erg s}^{-1} \text{ cm}^{-2} \text{ Hz}^{-1}$ , the value of the pre-reionisation UV background at  $z = 8$ , according to the Haardt & Madau model) for the gas at densities above  $n = 0.1 \text{ cm}^{-3}$ . This density threshold is motivated by radiative transfer calculations (appendix A1 of Fumagalli et al. 2011, figure A2).

Our special version of the ART code has a unique feature for the purpose of simulating the detailed structure of the streams. It allows gas cooling to well below  $10^4 \text{ K}$  so enabling the formation of high densities in pressure equilibrium with the hotter and more dilute medium. A non-thermal pressure floor has been implemented to ensure that the Jeans length is resolved by at least seven resolution ele-

ments and thus prevent artificial fragmentation on the smallest grid scale (Truelove et al. 1997; Robertson & Kravtsov 2008; Ceverino, Dekel & Bournaud 2010). It is effective in the dense ( $n > 10 \text{ cm}^{-3}$ ) and cold ( $T < 10^4 \text{ K}$ ) regions inside galactic disks.

The equation of state remains unchanged at all densities. Stars form according to a stochastic model that is described in appendix A of Ceverino & Klypin (2009). The SFR surface density and the gas surface density are measured from the simulations and compared with the Kennicutt relation in the appendix A of Ceverino et al. (2014), figure A1. The stochastic star formation model reproduces the Kennicutt (1998) law. This happens in cells where the gas temperature is below  $10^4 \text{ K}$  and the gas density is above a threshold of  $n = 1 \text{ cm}^{-3}$ . We use the IMF from Miller & Scalo (1979) that is also matching the results of Woosley & Weaver (1995). Metals from supernovae type II and type Ia enrich the ISM. They are released from each star particle by SNII at a constant rate for 40 Myr after its birth. The metal ejection by SNIa assumes an exponentially declining SNIa rate from a maximum at 1 Gyr. The code treats the advection of metals self-consistently and it distinguishes between SNII and SNIa ejecta (Ceverino-Rodriguez 2008).

### 2.1.1 Simulations including radiation pressure ( $A_{\text{RP}}$ )

The  $A_{\text{RP}}$  suite of simulations (Ceverino et al. 2014) is a further development of last subsection’s ART suite: apart from the features already presented there, it also includes the effects of radiation pressure by massive stars. The radiation pressure was modelled as a non-thermal pressure that acts only in dense and optically thick star-forming regions in a way that the ionising radiation injects momentum around massive stars, pressurising star-forming regions (Agertz et al. 2013, their appendix B). The adaptive comoving mesh has been refined in the dense regions to cells of minimum size between 17-35 pc in physical units. The DM particle mass is  $8.3 \times 10^4 M_{\odot}$ . The particles representing star clusters have a minimum mass of  $10^3 M_{\odot}$ , similar to the stellar mass of an Orion-like star cluster.

## 2.2 Ramses Horizon-MareNostrum simulation

The AMR code RAMSES (Teyssier 2002) is used for this simulation. Its spatial resolution in physical units is  $\sim 1 \text{ kpc}$ . We included UV heating via a background model (Haardt & Madau 1996). Supernovae feedback and metal enrichment are modelled in a simple way using the implementation described in Dubois & Teyssier (2008). Cooling rates are calculated assuming ionisation equilibrium for H and He, for collisional- and photo-ionisation (Katz, Hernquist & Weinberg 1992). Metal cooling is assumed to be proportional to the metallicity, relative to the solar abundance (Grevesse & Sauval 1998). It is calculated with the help of tabulated CLOUDY rates. Unlike in the ART or  $A_{\text{RP}}$  simulations, no cooling below  $T < 10^4 \text{ K}$  is computed, and no self-shielding of the UV flux is assumed.

For high-density regions, we consider a polytropic equation of state with  $\gamma_0 = 5/3$  to model the complex, turbulent multi-phase structure of the inter-stellar

label	suite	$M_{\text{vir}} [10^{12} M_{\odot}]$	$z$	$N_{\text{gal}}$
$10^{13}$	MN	$10.47 \pm 0.56$	1.57	12
$10^{13}$	MN	$10.49 \pm 0.93$	2.46	12
$5 \times 10^{12}$	MN	$5.00 \pm 0.045$	1.57	12
$5 \times 10^{12}$	MN	$5.48 \pm 0.26$	2.46	11
$10^{12}$	MN	$1.03 \pm 0.003$	1.57	8
$10^{12}$	MN	$1.01 \pm 0.004$	2.46	12
$10^{12}$	MN	$1.03 \pm 0.006$	4.01	9
$10^{11}$	MN	$0.099 \pm 0.000$	1.57	12
$10^{11}$	MN	$0.099 \pm 0.000$	2.46	7
$10^{11}$	MN	$0.099 \pm 0.000$	4.01	12
$1.9 \times 10^{12}$	ART	$1.907 \pm 0.217$	$1.14 \pm 0.02$	34
$1.3 \times 10^{12}$	ART	$1.286 \pm 0.093$	$1.60 \pm 0.02$	73
$8.6 \times 10^{11}$	ART	$0.863 \pm 0.046$	$2.25 \pm 0.02$	109
$3.9 \times 10^{11}$	ART	$0.391 \pm 0.034$	$3.40 \pm 0.04$	119
$7.1 \times 10^{11}$	$A_{\text{RP}}$	$0.707 \pm 0.055$	$1.14 \pm 0.02$	41
$6.7 \times 10^{11}$	$A_{\text{RP}}$	$0.672 \pm 0.049$	$1.58 \pm 0.02$	47
$4.9 \times 10^{11}$	$A_{\text{RP}}$	$0.491 \pm 0.028$	$2.21 \pm 0.03$	57
$2.9 \times 10^{11}$	$A_{\text{RP}}$	$0.290 \pm 0.019$	$3.27 \pm 0.05$	62
$2.6 \times 10^{11}$	$A_{\text{RP}}$	$0.260 \pm 0.010$	$1.13 \pm 0.02$	40
$2.4 \times 10^{11}$	$A_{\text{RP}}$	$0.242 \pm 0.010$	$1.59 \pm 0.02$	50
$1.6 \times 10^{11}$	$A_{\text{RP}}$	$0.160 \pm 0.007$	$2.29 \pm 0.03$	60
$7.3 \times 10^{10}$	$A_{\text{RP}}$	$0.073 \pm 0.004$	$3.53 \pm 0.05$	66

**Table 1.** The different bins of galaxies which are used throughout this paper. ‘Label’ denotes the tag a bin is labelled with in any of the figures. It usually is a mass very close to the ensemble’s actual mean virial mass. ‘Suite’ indicates the simulation set the bin consists of.  $M_{\text{vir}}$  gives the actual mean virial mass of the ensemble together with its standard deviation.  $z$  is the mean redshift of the ensemble together with its standard deviation. We do not combine galaxies from different MN snapshots therefore the standard deviation of the redshift of any of the MN bins is always zero.  $N_{\text{gal}}$  is the number of galaxies in the respective bin.

medium (ISM) (Yepes et al. 1997; Springel & Hernquist 2003) in a simplified form (see Schaye & Dalla Vecchia 2008; Dubois & Teyssier 2008). The ISM is defined as gas with hydrogen density greater than  $n_{\text{H}} = 0.1 \text{ cm}^{-3}$ . This definition is one order of magnitude lower than the one of the ART and  $A_{\text{RP}}$  simulations. Star formation only for ISM gas has been included. It is modelled by spawning star particles at a rate consistent with the Kennicutt (1998) law derived from local observations of star forming galaxies.

The RAMSES code implements a pressure floor in order to prevent artificial fragmentation, by keeping the Jeans lengthscale,  $\lambda_{\text{J}} \propto Tn^{-2/3}$ , larger than four grid-cell sides everywhere. In any case where  $n > 0.1 \text{ cm}^{-3}$ , a density dependent temperature floor was imposed. It mimics the average thermal and turbulent pressure of the multiphase ISM (Springel & Hernquist 2003; Dalla Vecchia & Schaye 2008). In our case, we allow the gas to heat up above this temperature floor and cool back. The temperature floor follows a polytropic equation of state with  $T_{\text{floor}} = T_0(n/n_0)^{\gamma_0-1}$ , where  $T_0 = 10^4 \text{ K}$  and  $n_0 = 0.1 \text{ atoms cm}^{-3}$ . The resulting pressure floor is given by  $P_{\text{floor}} = n_{\text{H}}k_{\text{B}}T_{\text{floor}}$ . For each stellar population, 10% of the mass is assumed to go through a supernovae type II event after 10 Myr. For each supernova, 10% of the ejected mass is assumed to be pure metals. The energy and the metals produced by the supernova event are released in a single impulse. The remaining 90% of the



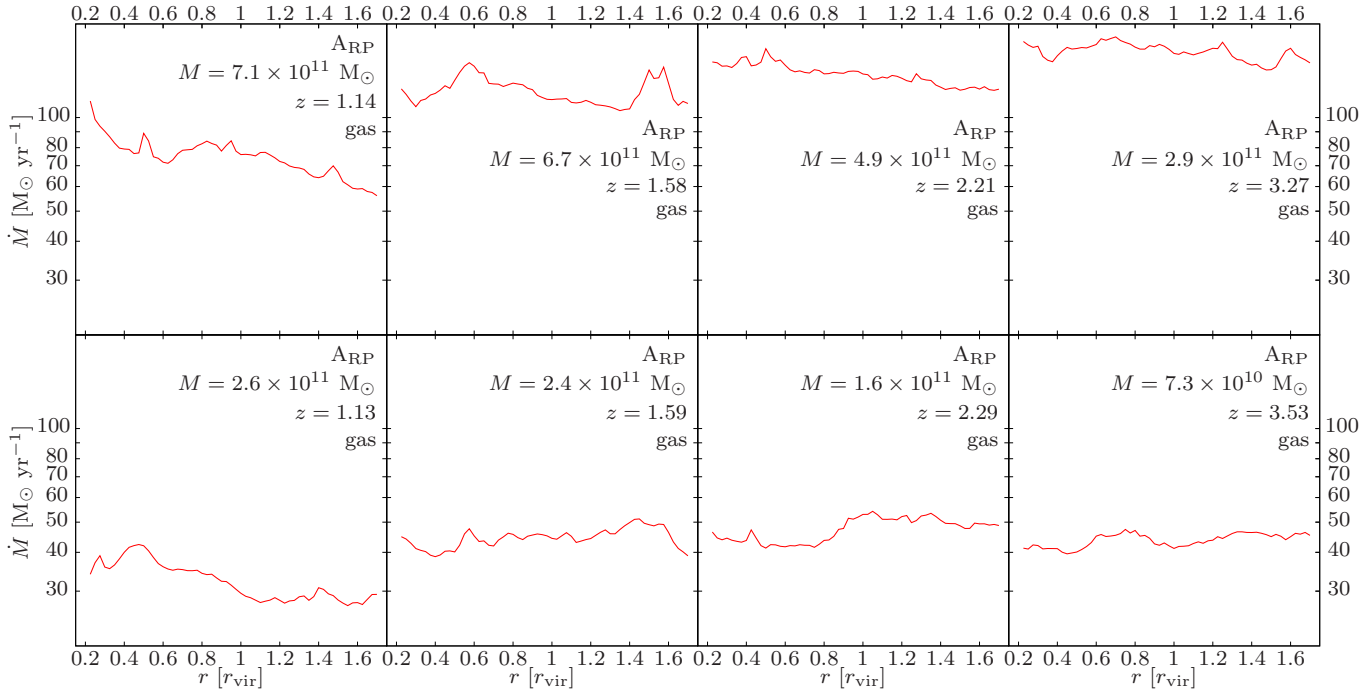


**Figure 2.** Average inflow as a function of radius for different halo masses and redshifts for the ARP simulations. The different panels indicate a variety of different halo masses and redshifts. The inflow in gas is remarkably constant with radius, except for the higher mass very low redshift panel, which has a very mildly declining mass accretion with increasing radius. However by and large the mass accretion rate of gas is constant with radius.

ejected mass keep the metallicity of their star at birth. Feedback through supernovae type Ia has not been considered.

The initial conditions were constructed assuming a  $\Lambda$ CDM universe with  $\Omega_M = 0.3$ ,  $\Omega_\Lambda = 0.7$ ,  $\Omega_b = 0.045$ ,  $h = 0.7$  and  $\sigma_8 = 0.9$  in a periodic box of 71 Mpc. The adaptive-resolution rules in this simulation were the same everywhere, with no zoom-in resimulation of individual galaxies. The dark matter particle mass is  $1.16 \times 10^7 M_\odot$ , the star particle mass is  $2.05 \times 10^6 M_\odot$ , the smallest cell size is 1.09 kpc physical, and the force softening length is 1.65 kpc.

We will show averaged results for an ensemble of galaxies having very similar masses and redshifts. In table 1 we show a summary of the various bins of galaxies we use. Since we have better statistics for the MN simulation we could bin galaxies from a narrower mass range therefore the standard deviations of the mean mass of a MN bin is usually much smaller. To partly compensate for that we combine ART as well as ARP galaxies from adjacent redshifts increasing the statistics but introducing a standard deviation into the mean redshift of the bin.

### 3 MASS ACCRETION RATE

In a companion paper (Goerdt et al. 2015) we look at the amount of inflow – the mass accretion rate – both as a function of radius, mass and redshift for the three constituents gas, stars and dark matter. Since the mass accretion rate of the gas is ultimately what is interesting for the rate of star formation and how much gas needs to be lost via outflows

we show briefly an analysis of the mass accretion rate of the gas in this section.

The analysis of the ARP simulations starts by looking at the average gas inflow as a function of radius: We measure the amount of mass which is crossing a spherical shell of radius  $r$  centred around a given individual galaxy within a small time  $\Delta t$ . The mass crossing the shell is divided by the time taken ( $\Delta t$ ) to get an inflow rate. In order to get the best estimate for the inflow in case of gas we decided to take into account only the cells which have an inwards radial velocity. In order to get rid of the statistical noise of a single galaxies we average the amount of inflow over all available galaxies having similar redshifts and masses.

The amount of inflow into the galaxies as a function of radius is shown in figure 2. The magnitude of the inflow is basically constant over all radii  $r$  regardless of the actual mass-redshift bin, except for the one higher mass very low redshift panel, which has a very mildly declining mass accretion with increasing radius. However by and large the amount of inflow is constant with radius. So we can mainly see that the mass accretion rate simply follows the velocity profile, i.e. cold and hot gas are not mixed as it falls in. As already mentioned we discuss these trends and also the mass accretion rates of stars and dark matter in a companion paper (Goerdt et al. 2015).

### 4 ANALYTICAL MODELS

Naively one would expect the gas inflow velocities to obey one of the following two quantities: either free-fall or the sound speed of the hot ambient medium. The underlying as-

sumption of the first case is that the gas flows freely within the gravitational potential into its host and is otherwise completely unconstrained. In the second case one assumes that the velocity of the gas will be fundamentally limited by the sound speed of the hot ambient medium through the effect of shocks which occur within the streams themselves as well as at the boundary layers between the streams and the hot ambient medium as soon as the velocity of the inflowing gas reaches the sound speed of this ambient medium.

#### 4.1 Free-fall

Free-fall profiles cannot be calculated analytically. To evaluate them numerically we follow the method laid out by Rosdahl & Blaizot (2012) which we will quickly outline here: a static, spherically symmetric potential is assumed. We integrate the free-fall speeds  $v_{\text{ff}}(r)$  from a starting position  $r_0$  and a starting velocity  $v_{\text{init}} = v_{\text{ff}}(r_0)$  towards the halo centre using

$$dv_{\text{ff}}(r) = \frac{1}{v_{\text{ff}}(r)} \frac{G M(< r)}{r^2} dr, \quad (1)$$

where  $r$  is radius,  $M(< r)$  is the total halo mass within  $r$  and  $G$  is the gravitational constant. In practice we divide the host halo into spherical bins at radial positions  $r_i$ , where an increasing  $i$  corresponds to a decreasing radius, and solve the above equation by recursively computing

$$v_{\text{ff}}(r_{i+1}) = v_{\text{ff}}(r_i) + \frac{1}{v(r_i)} \frac{G M(< r_{i+1})}{r_{i+1}^2} (r_{i+1} - r_i). \quad (2)$$

The underlying mass distribution  $M(< r_{i+1})$  is measured from the outputs of the hydrodynamical simulations as described in section 2. We choose an initial position ( $r_0 = 1.7 r_{\text{vir}}$ ) as well as an initial inward velocity ( $v_{\text{init}} = 0$ ) and integrate the path of the free-falling gas iteratively until a very small radius ( $0.1 r_{\text{vir}}$ ) is reached. The free-fall profiles usually show a strongly increasing velocity with decreasing radius. The results of the calculations are presented in detail in section 5. We will see that these predictions violently disagree with the results from the hydrodynamical simulations.

#### 4.2 Sound speed of the ambient medium

The sound speed  $c_s$  of the hot ambient halo gas on the other hand can be calculated analytically. Sound speed as such equals to

$$c_s(\vec{r}) = \sqrt{\frac{\gamma k_B T(\vec{r})}{m_p \mu_{\text{av}}}}, \quad (3)$$

with  $\gamma$  being the ratio of the heat capacity at constant pressure to the heat capacity at constant volume, which is usually a constant ( $\sim 5/3$ ).  $k_B$  is Boltzmann's constant,  $m_p$  is the proton mass,  $\mu_{\text{av}}$  is the mean molecular weight (for ionised gas  $\mu_{\text{av}} = 0.61$ ) and  $T(\vec{r})$  is temperature of the gas as a function of position.

##### 4.2.1 Approximated constant halo gas temperature

For a first order approximation the temperature of the ambient halo gas is assumed to be equal to the virial temperature of the host halo. It is constant with position and given by

$$T_{\text{vir}} = \frac{G M_{\text{vir}} m_p \mu_{\text{av}}}{2 r_{\text{vir}} k_B}. \quad (4)$$

$G$  is the gravitational constant,  $M_{\text{vir}}$  is the virial mass of the host halo and  $r_{\text{vir}}$  its virial radius. These three quantities are related via

$$v_{\text{vir}} = \sqrt{\frac{G M_{\text{vir}}}{r_{\text{vir}}}}. \quad (5)$$

After inserting the expressions for  $T_{\text{vir}}$  and  $v_{\text{vir}}$  into equation (3) we get an expression for the sound speed. Assuming that the velocity of the gas in the cold streams indeed equals to the sound speed of the ambient medium, because the shocks which occur as soon as the inflow velocity reaches the sound speed will fundamentally limit the velocity of the gas one gets a first order approximation for the infall velocity:

$$v_{\text{inflow}} = 0.913 v_{\text{vir}} \quad (6)$$

In this approximation the infall velocity is constant with radial distance from the host halo. We will come back to this statement at the end of section 5 where we will see that this particular equation tends to be accurate for very high redshift haloes ( $z \gtrsim 4.0$ ) and more importantly that the infall velocity is in general indeed constant with radius.

##### 4.2.2 Simulated halo gas temperature

A more sophisticated measure of the ambient medium's temperature is not to approximate the gas temperature anymore, but to measure it directly from the hydrodynamic simulations as a function of position. Since we assume spherical symmetry it is sufficient to measure it as a function of radial distance from the host halo centre. When looking at the simulations one has to carefully discriminate between the gas of the ambient medium which is hot and the gas flowing into the host as part of the cold streams which is cold. Only the temperatures of the ambient medium will determine the velocity of the cold streams. To distinguish between cold streams on the one hand and hot halo gas on the other hand we adopt the following temperature cut: temperatures are defined as 'hot' in this sense if they are at least  $> 0.2 T_{\text{vir}}$  or  $> 3 \times 10^4$  K whatever is the higher value. The mass weighted average temperatures of the hot ambient halo gas only are then taken in spherically symmetric bins at different radii  $r$  to get a numerical temperature profile  $T(r)$ . Inserting this numerical profile for the temperature into equation (3) we get a sound speed profile for each set of simulated galaxies that are listed in table 1. The sound speed profiles are presented together with the results from the hydrodynamical simulations in section 5. For the MN simulations at intermediate to high masses ( $M_{\text{vir}} \geq 10^{12} M_{\odot}$ ), the sound speed is increasing with decreasing redshift almost as sharply as the free-fall profiles. In these regions of the parameter space it can only serve as a slightly better proxy for the inflow velocity than free-fall. In all four bins of the ART simulations the sound speed profiles increase slightly with decreasing radius. In case of the ART simulations the sound speeds match the simulations very precisely as we will see later in figure 4. The profiles increase slightly with decreasing radius also in the ARP simulations. Their shape is very similar to the actual simulation values but the sound speeds are usually 50% higher than the simulation values. To summarise: the sound speed of the hot ambient

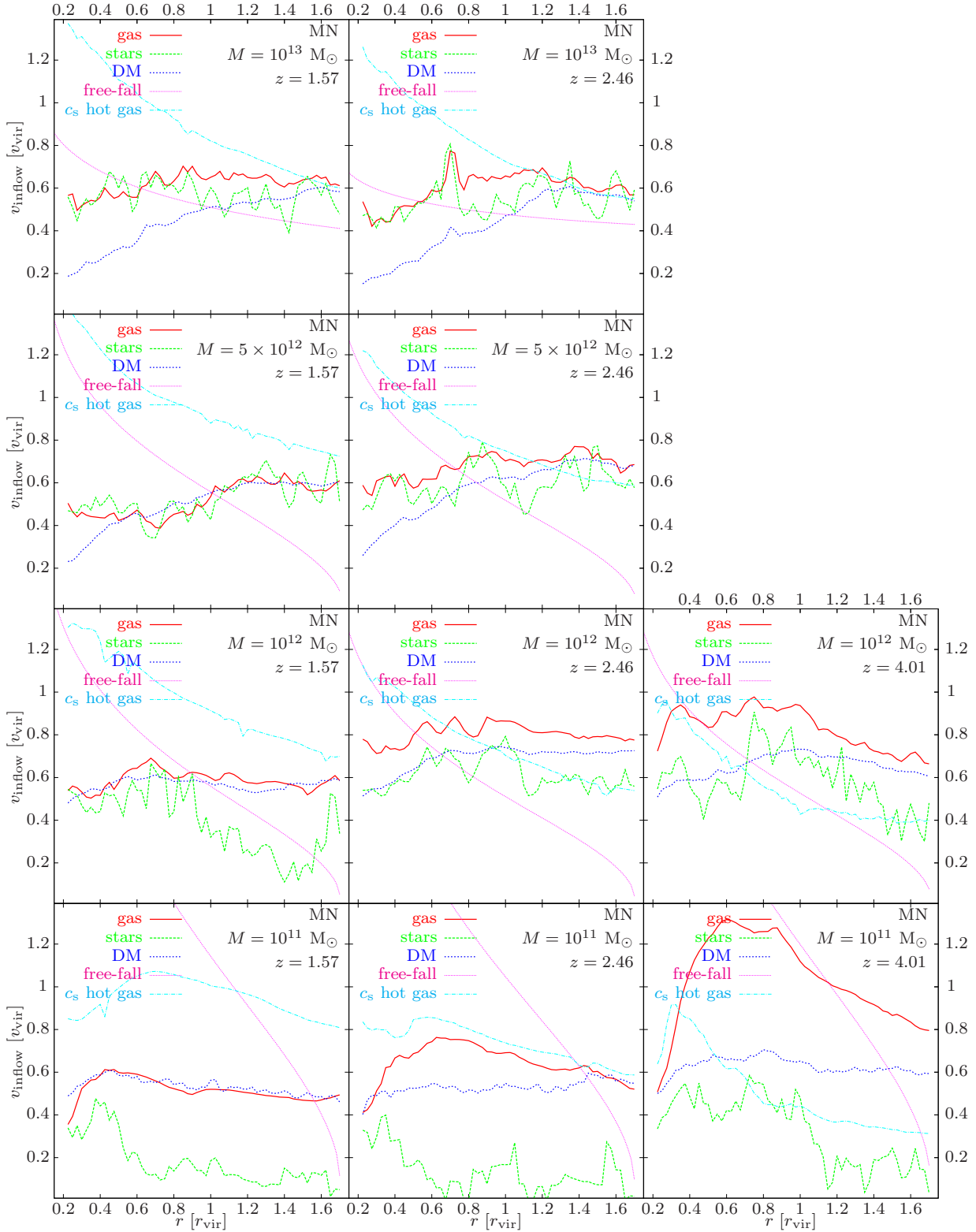


**Figure 3.** Mass weighted averages of the inflow velocities as a function of radius for the MN simulations. The different panels indicate a variety of different halo masses and redshifts. Corresponding free-fall profiles are over-plotted in dotted magenta and profiles of the sound speed of the hot ambient halo gas in dash-dotted turquoise. For low mass haloes ( $M_{\text{vir}} \leq 10^{12} M_{\odot}$ ) at all redshifts the velocities are roughly constant with radius. For high mass haloes ( $M_{\text{vir}} \geq 5 \times 10^{12} M_{\odot}$ ) the inflow velocities increase slightly with increasing radius. Subsequently no sign of free-fall can be seen in any of the bins. In the very high redshift and low mass cases one sees an increase of velocity with decreasing radius down to  $0.6 r_{\text{vir}}$  from where the velocity is decreasing again. These shapes are typical for high redshift low mass haloes. In units of the virial velocity the average inflow velocity stays roughly constant with varying host halo mass, it increases with an increase in redshift.

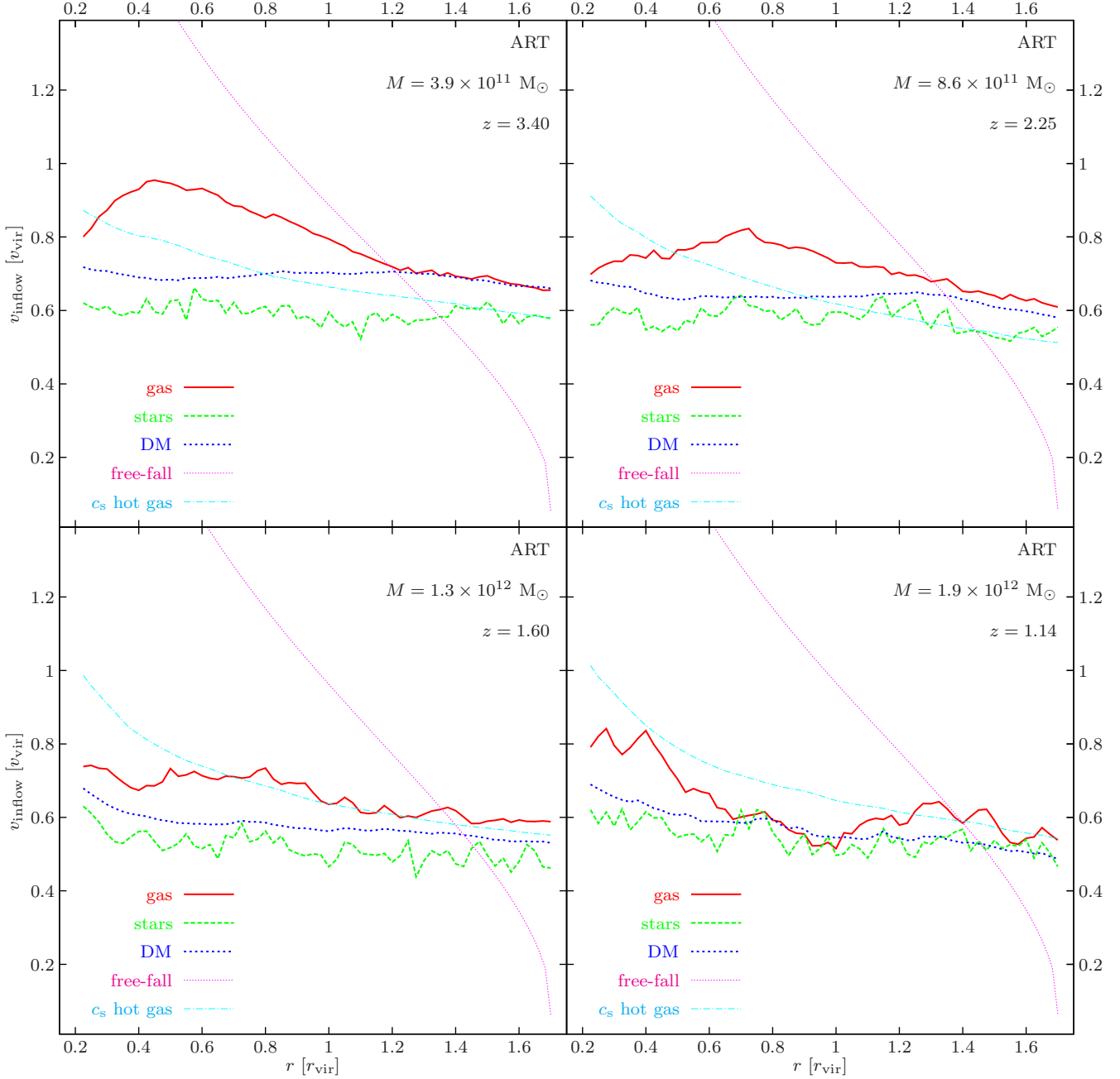


**Figure 4.** Mass weighted averages of the inflow velocities as a function of radius for the ART simulations. Free-fall profiles are over-plotted in dotted magenta and the sound speeds of the hot ambient halo gas in dash-dotted turquoise. The inflow velocities of the gas increase slightly with decreasing radius. The total increase over the whole radius range is usually roughly 50%. These increases however are not consistent with free-fall as the corresponding profiles show. The sound speeds of the hot halo gas are a much better proxy, at least at high redshift. In the higher redshift cases one sees an increase of velocity with decreasing radius down to  $\sim 0.5 r_{\text{vir}}$  from where the velocity is decreasing again. A shape like that is typical for low mass haloes at high redshift, it originates in the loss of angular momentum during the “strong-torque phase” (Danovich et al. 2015).

halo gas is a better proxy for the velocity of the inflow than free-fall. It is more precise at low masses ( $M_{\text{vir}} \leq 10^{12} M_{\odot}$ ) and gives very good results for the ART suite of simulations. However it is only an incomplete prescription for the inflow velocity.

## 5 INFLOW VELOCITIES

The analysis of the hydrodynamical simulation starts by compiling averaged inflow velocity profiles for all simulated galaxies listed in table 1. Since we want to look at the velocities of the inflowing cold streams and not at the average velocity of some net inflow we have to discriminate between the inflowing material belonging to the cold streams and



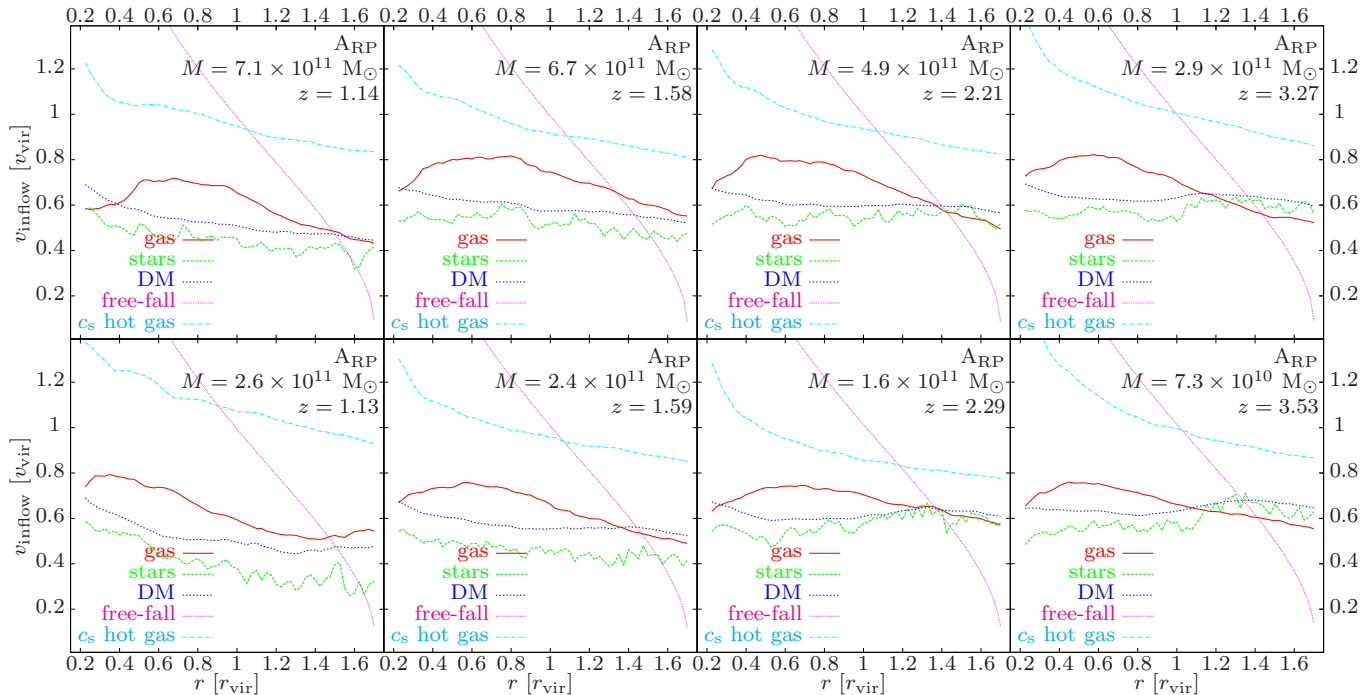


**Figure 5.** Mass weighted averages of the inflow velocities as a function of radius for the ARP simulations. Free-fall profiles are over-plotted in dotted magenta and the sound speeds of the hot ambient halo gas in dash-dotted turquoise. Again the inflow velocities of the gas increase with decreasing radius in most cases. These increases are again not consistent with free-fall. In most cases one sees an increase of velocity with decreasing radius down to  $\sim 0.5 r_{\text{vir}}$  from where the velocity is decreasing again. A shape like that is typical for low mass haloes at high redshift.

the ambient halo material. We experimented with different cuts and found out that a simple inflow criterion should be sufficient. Since different gas phases are reported to have very different accretion properties (Nelson et al. 2013) and we want to concentrate on the kinematics of the cold flows only we decided to adopt for the gas an additional temperature cut of  $T < 3 \times 10^4$  K. So the velocities are computed for gas by averaging the radial velocity component of all inflowing cells having temperatures less than  $3 \times 10^4$  K in a given radius bin. The dark matter and stellar velocities are computed for by averaging the radial velocity component of all inflowing particles in a given radius bin. Only cells and particles with negative radial velocities and only cells with temperatures less than  $3 \times 10^4$  K are taken into account, i.e. all motion perpendicular to the radial infall direction as well as all cells or particles which are moving outwards as well as all cells with temperatures higher than  $3 \times 10^4$  are completely neglected. The resulting values are averaged over all available galaxies in the respective mass and redshift bin. Velocities are always quoted dimensionless, namely in units of the virial velocity  $v_{\text{vir}}$  which has already been defined in equation (5).

The resulting inflow velocity profiles are shown in figures 3 (MN), 4 (ART) and 5 (ARP). Free-fall profiles are over-plotted in dotted magenta and the sound speeds of the ambient gas is over-plotted in dash-dotted turquoise. The most striking feature visible is that the velocity is to a very good approximation constant with radius. It is clearly not free-falling. This is the case for all three suites of simulations, for all redshifts or masses as well as for all three constituents: gas, stars or dark matter. The potential energy of

the inflowing gas is not converted into kinetic energy, it has to be dissipated by another mechanism, most likely by  $\alpha$ -radiation (Goerdts et al. 2010). In some of the cases however the velocity of the gas follows the sound speed profiles of the hot ambient medium fairly well.

Looking at the graphs more carefully the following deviations from constant velocity infall can be found: MN’s high mass haloes ( $M_{\text{vir}} \geq 5 \times 10^{12} M_{\odot}$ ) have decreasing inflow velocities with decreasing radius. In most of the ART and ARP galaxies on the other hand an increase of the velocity can be seen as the material falls further in. This infall however is far from being consistent with free-fall as the overlain profiles demonstrate. In all other cases the inflow velocity is indeed constant.

Additionally there is a dependency of the shape of the infall velocity profiles with mass and redshift: For low mass haloes ( $M_{\text{vir}} \leq 5 \times 10^{12} M_{\odot}$ ) at high redshift ( $z \gtrsim 1.7$ ) usually there is an increase of velocity with decreasing radius down to  $\sim 0.5 r_{\text{vir}}$  from where the velocity is decreasing again. This behaviour originates in the loss of angular momentum due to strong torques in a tilted extended ring, the “strong-torque phase” of the inflow (Danovich et al. 2015, their section 5 and figure 20). For very high mass haloes ( $M_{\text{vir}} > 2.5 \times 10^{12} M_{\odot}$ ) the inflow velocity is slightly increasing with increasing radius over the whole radius range without ever turning down again. In the remaining bins the inflow velocity is constant or only very mildly increasing with decreasing radius also over the whole radius range also without ever turning down again.

The velocities of the star particles with negative radial velocities stay remarkably constant over the whole radius

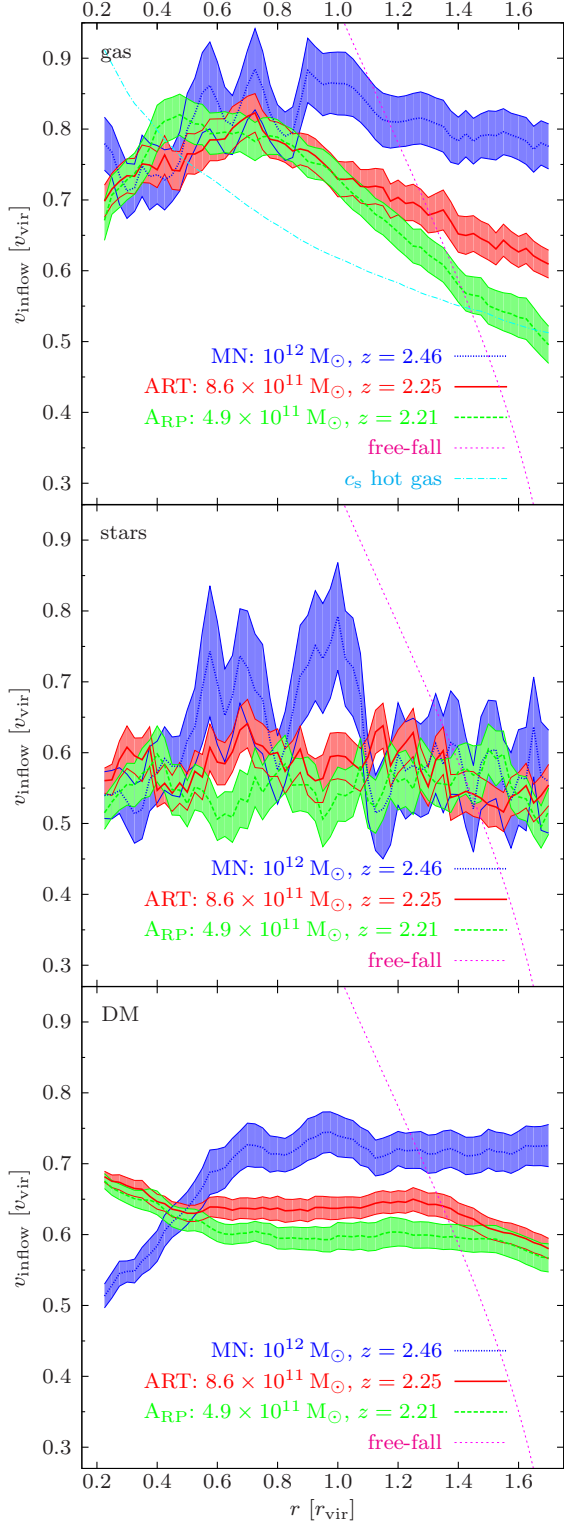


**Figure 6.** Direct comparison between the MN (dotted blue), the ART (solid red) and the  $A_{RP}$  (long-dashed green) suite of simulations. The inflow velocities as a function of radius are shown together with their  $1\sigma$  standard deviation lines. Over-plotted are a free-fall profile (short-dashed magenta) and the sound speed of the hot ambient halo gas  $c_s$  (dash-dotted turquoise). Inflow velocities for MN, ART and  $A_{RP}$  roughly agree with each other within the  $1\sigma$  standard deviation, small offsets can be accounted for by the slightly different redshifts.

range for all masses and redshifts. The velocities of the dark matter particles with negative radial velocities increase with increasing radius for high mass galaxies ( $> 3 \times 10^{12} M_{\odot}$ ) and decrease with increasing radius for low mass galaxies ( $< 3 \times 10^{12} M_{\odot}$ ). One would naively expect that at least the dark matter particles inflow velocities would follow free-fall, since those are collision-less and therefore cannot be slowed down by any baryonic processes. However there is no meaningful dark matter accretion within  $\sim 2 r_{\text{vir}}$  as already pointed out by Cuesta et al. (2008) or Wetzel & Nagai (2014). Therefore the dark matter particles are not inflowing within the radius range analysed, they are just moving in and out again of a certain innermost sphere since the halo is virialised and most of the dark matter particles are orbiting on non-circular orbits.

The finding of constant velocity inflow is in contrast to earlier works (Faucher-Giguere et al. 2010; Rosdahl & Blaizot 2012). These authors report evidence for free-fall behaviour of the cold streams. A possible explanation for the discrepancies with Faucher-Giguere et al. (2010) might be, that they deployed SPH simulations which used to have inaccuracies modelling dissipative processes (Agertz et al. 2007). Such processes are taking place frequently at the boundary layers of cold streams. Also Nelson et al. (2013) found differences in the accretion properties for different hydro schemes. Rosdahl & Blaizot (2012) on the other hand used AMR techniques, like us. Their sample of galaxies however was small (only three galaxies in total) and they report that not all of their galaxies showed signs of free-fall behaviour. Constant velocity inflow on the other hand is in agreement with the results from Teklu (2012). She finds constant velocity profiles at around  $170 \text{ km s}^{-1}$  for three galaxies with  $M_{\text{vir}} = 1.5 \times 10^{12} M_{\odot}$  at  $z = 2.33$  in her simulations. Roughly constant velocity inflow is also in agreement with the results of van de Voort & Schaye (2012), their absolute velocities of  $150 \text{ km/s}$  ( $\sim 0.75 v_{\text{vir}}$ ) is remarkably close to the values we found ( $\sim 0.7 v_{\text{vir}}$ ). Also Nelson et al. (2015b) find roughly constant inflow velocities, c.f. their figure 7. Strictly non free-falling inflow is also in agreement with the results from Wetzel & Nagai (2014), their figures 4 and 6) who see a decrease in velocity with decreasing radius (roughly a decrease of 65% between  $1 r_{\text{vir}}$  and the centre of the host). Unlike us they did not exclude outflowing cells and particles which explains their velocities that are varying with radius as well as the on average lower values of their speeds.

To guarantee the consistency of the MN, the ART and the  $A_{RP}$  simulations it is necessary to compare them directly. In figure 6 galaxies at  $z \sim 2.3$  with  $M_{\text{vir}} \sim 8 \times 10^{11} M_{\odot}$  are shown for the three suites of simulations. The lines for stars and dark matter are very similar for all three: the velocities are roughly constant over the whole radius range at comparable values. However the gas curves are slightly different: the MN one is by and large constant, whereas the ART as well as the  $A_{RP}$  one increase slightly with decreasing radius. The overall increase is roughly 35% over the whole radius range ( $1.7 - 0.2 r_{\text{vir}}$ ). These increases, as mentioned earlier, are not consistent with free-fall. There is an offset in the values: the MN velocities are  $\sim 30\%$  higher over most of the radius range. The offset can be accounted for by the offsets, which the host haloes' masses and redshifts have.

Nelson et al. (2015a) found that feedback affects gas ac-

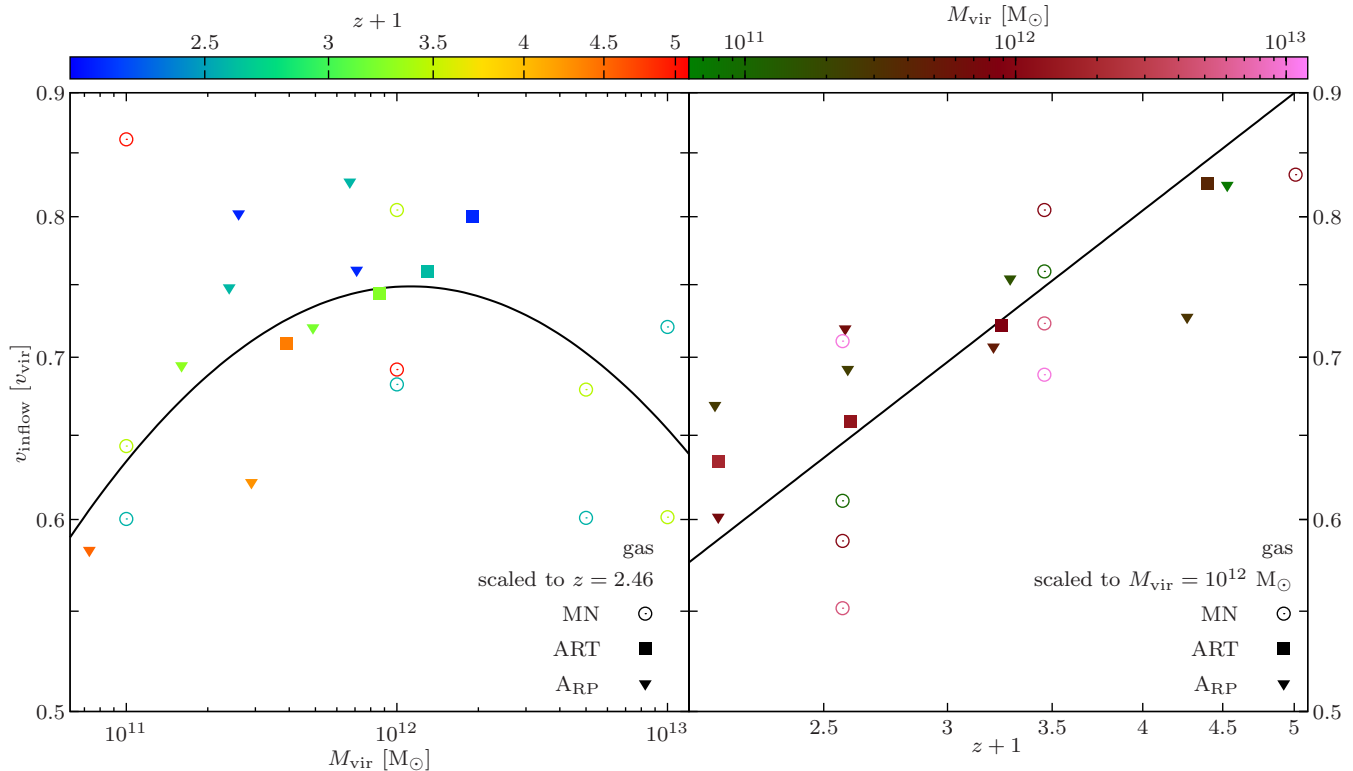


**Figure 7.** Average inflow velocity  $v_{\text{inflow}}$  in units of the virial velocity as a function of virial mass  $M_{\text{vir}}$  (left) or as a function of redshift  $z + 1$  (right). There is a strong square root power law relationship between the inflow velocity and the redshift (right panel). The inflow velocity also follows a “parabola-like” relation with respect to the host halo mass on the other hand that peaks roughly at  $M_{\text{vir}} = 10^{12} M_{\odot}$  (left panel). The data points within each panel were scaled with the help of the scaling relation in the respective other panel to the values indicated. Both scaling relations were found together in an iterative process (see text). The colour bar axes indicate the values the data points used to have before rescaling.

cretion. Our three suites of simulations use varying strengths of feedback. As we can see from figure 6 varying strengths of feedback affect the inflow velocities only very mildly. However as we will discuss in our forthcoming companion paper (Goerdt et al. 2015) varying strengths of feedback do affect the total amount of inflow.

After the consistency of the infall velocities in all three suites of simulations has been established one can now look at possible trends of the infall velocities with mass and redshift. We want to quantify the qualitative statements made earlier. For simplicity a constant infall velocity with radius is assumed. Its actual value is determined by a constant line fit through the velocity curve of the respective mass-redshift bin.

The average inflow velocities  $v_{\text{inflow}}$  of the gas are shown as a function of halo mass  $M_{\text{vir}}$  and redshift  $z + 1$  in figure 7. Plotted are in both panels all available bins of galaxies from MN, ART and ARP as listed in table 1. In the left panel the  $v_{\text{inflow}}$  values are plotted against the halo mass ( $M_{\text{vir}}$ ) and in the right panel against redshift  $z + 1$ . One can easily identify that the  $v_{\text{inflow}}$  values in the right panel follow a linear relation with respect to  $z + 1$  on this log-log graph, which is a power law. Since in this case the exponent is remarkably close to a half we decided in order to reduce the number of free parameters of our fitting function to choose a square root power law as the fitting function for the  $v_{\text{inflow}}$  values with respect to  $z + 1$ . The best fit square root power law is

over-plotted by the solid black line. The  $v_{\text{inflow}}$  values in the left panel however seem to follow a “parabola-like” function on this log-log graph, which is the log-normal distribution function. We choose this function because the parabola is the simplest function with a non-constant derivative, i.e. the simplest function which rises first and declines later. Since we are working in log-log space we had to go with its log-log analogue, the log-normal distribution function. The function peaks at  $M_{\text{vir}} = 10^{12} M_{\odot}$ . For the sake of simplicity we will refer to this kind of function as “parabola-like” throughout the paper.

The  $v_{\text{inflow}}$  values of most data points in both panels had to be rescaled in the following way: the  $v_{\text{inflow}}$  values of the data points within the left panel that were not at  $z = 2.46$  were scaled to this value according to the scaling relation presented in the right panel. Likewise the  $v_{\text{inflow}}$  values of the data points within the right panel whose underlying galaxy bins were not at  $M_{\text{vir}} = 10^{12} M_{\odot}$  had to be rescaled to that value according to the scaling relation presented in the left panel. The colour bar axes in both panels indicate the values the galaxy bins used to have before rescaling.

Both scaling relations were found in the following iterative process: first a square root power law was fit through the yet unrescaled data points in the right panel. This relation was then been used to rescale the data points in the left panel. Subsequently a log-normal distribution function was fit through the (scaled) data points in the left panel. Af-

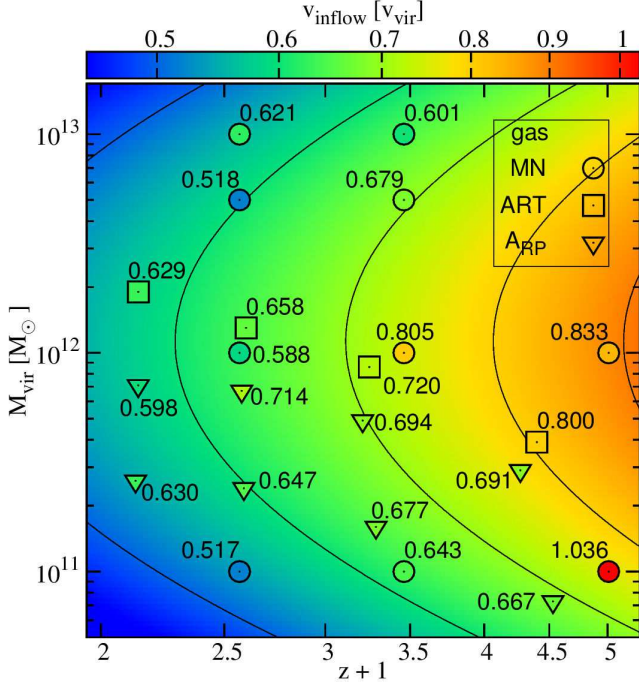


**Figure 8.** Average inflow velocity of the gas in units of the virial velocity as a function of halo mass and redshift. Shown as background colour is the fitting function (equation 7) with contour lines at 0.5, 0.6, 0.7, 0.8 and 0.9  $v_{\text{vir}}$ . The actual values measured from the simulations are given with colour coding within the open symbols as well as by the attached labels. ART is marked by squares, MN by circles and  $\text{ARP}$  by triangles.

terwards the resulting log-normal distribution function was used to rescale the data points in the right panel. These steps have been repeated until convergence was reached (i.e. until the resulting scaling relations did not change anymore). Convoluting the square root power law with the log-normal distribution function leads to the following equation which serves as a model describing the behaviour of the cold stream infall velocity as a function of redshift and host halo mass:

$$\frac{v_{\text{inflow}}(M_{\text{vir}}, z)}{v_{\text{vir}}(M_{\text{vir}}, z)} = \frac{A \sqrt{z+1}}{\sigma (M_{\text{vir}}/M_{\odot})} \times \exp \left\{ -\frac{[\ln(M_{\text{vir}}/M_{\odot}) - \mu]^2}{2\sigma^2} \right\} \quad (7)$$

Best fit parameter are  $A = (1.25 \pm 0.13) \times 10^{16}$ ,  $\mu = 45.4 \pm 4.8$  and  $\sigma = 4.20 \pm 0.53$ . A visualisation of this 3D functional fit is shown in figure 8, where the values that are actually measured from the simulations are given by the colour within the open symbols as well as by the attached labels. The ART results are represented by squares, the  $\text{ARP}$  results by triangles and the MN results by circles. Shown as background colour is the fitting function (equation 7) with contour lines at 0.5, 0.6, 0.7, 0.8 and 0.9  $v_{\text{vir}}$ .

We are aware of the fact that the choice of a “parabola-like” function instead of another power law as a scaling relation for the data points in the left hand side panel of figure 7 hinges only on the four very high mass ( $M \geq 5 \times 10^{12} M_{\odot}$ ) data points of the MN simulation which is the one having the lowest resolution. We decided to trust these data points

anyway since they were at the high mass end of our collection of galaxies where resolution issues play only a minor role. Unfortunately they were no ART or  $\text{ARP}$  galaxies available in this mass range. On the other hand we decided to neglect the MN data point at  $M_{\text{vir}} = 10^{11} M_{\odot}$  and  $z = 4.01$  having a very high inflow velocity as an outlier since it has a very low mass, so it might be more prone to resolution effects.

We are also aware of the fact that our choice of functional forms for equation (7) as well as figures 7 and 8 the square root power law on the one hand and the log-normal distribution on the other hand might seem to be very specific and arbitrary but those are the log-log analogues of the simplest functional forms having constant and non-constant derivatives, the straight line and the parabola. It is surely possible to find other functional forms which would lead to a different equation (7), but due to the constraining power of the data points those alternative functional forms should ultimately arrive at very similar predictions (i.e. the almost same appearance of figure 8) but they will have more free parameters.

## 6 CONCLUSIONS

In this paper we looked at the radial inflow velocities of accretion along streams from the cosmic web into massive galaxies at high redshifts using three sets of AMR hydrocosmological simulations. We calculated free-fall profiles as well as sound speeds of the hot ambient medium via two different methods and we found the following:

- The velocity profiles for the cold streams in the simulations are very different from free-fall.
- Not even the infall velocities of the dark matter particles follow free-fall, since there is no meaningful dark matter accretion within  $\sim 2 r_{\text{vir}}$  of the central halo (Cuesta et al. 2008; Wetzel & Nagai 2014). Therefore the dark matter particles are not inflowing they are rather moving back and forth.
- The sound speed of the ambient medium is a better proxy for the behaviour of the gas inflow velocity, at least at high redshifts. We present a neat scaling relation for the inflow velocity based on this as a first order approximation ( $v_{\text{inflow}} = 0.9 v_{\text{vir}}$ ).
- The velocity profiles for the cold streams are by and large constant with radius or only very slowly increasing with decreasing radius.
- There is a dependence of the shape of the gas infall velocity profiles with mass and redshift: for low mass haloes ( $M_{\text{vir}} \leq 5 \times 10^{12} M_{\odot}$ ) at higher redshift ( $z \gtrsim 1.7$ ) one usually sees an increase of velocity with decreasing radius down to  $\sim 0.5 r_{\text{vir}}$  from where the velocity is decreasing again. This originates in the loss of angular momentum during the “strong-torque phase” (Danovich et al. 2015).
- For very high mass haloes ( $M_{\text{vir}} > 2.5 \times 10^{12} M_{\odot}$ ) the inflow velocity is slightly increasing with increasing radius over the whole radius range. In all other cases the inflow velocity is constant or very mildly increasing with decreasing radius also over the whole radius range.
- This constant infall velocity has in units of the virial velocity as a function of radius a “parabola-like” dependency on the host halo mass that peaks at  $M_{\text{vir}} = 10^{12} M_{\odot}$  and it



also follows a square root power law relations with respect to the redshift ( $v_{\text{inflow}} \propto \sqrt{z+1} v_{\text{vir}}$ ).

• Since the magnitude of the mass accretion rate is also constant with radius one can follow that cold and hot gas do not mix as the cold streams fall in.

A potential limitation of our simulations could arise from the artificial pressure floor used in the simulations to ensure that the Jeans mass is always fully resolved. It might affect the temperature and density of the very dense and cold parts of the streams, with implications on the computed inflow velocities. Also the interaction between outflows and inflows is yet to be studied in simulations with strong feedback. Indeed preliminary results of House & Dekel (in preparation) show that there is no strong effect of strong feedback on to inflows. But AMR codes are still the best available tool for recovering the stream properties. With their 17 pc resolution, and with proper cooling below  $10^4\text{K}$ , these simulations provide the most reliable description of the cold streams that are available so far.

We conclude that the velocity profile of the gas flowing into a galaxy's halo in the form of cold streams is, contrary to what might be expected, roughly constant with radius instead of free-falling. The potential energy of the gas which is lost on its way is not converted into kinetic energy but must be dissipated by other mechanisms, such as  $\text{Ly}\alpha$  radiation (Goerdt et al. 2010).

## ACKNOWLEDGEMENTS

Tobias Goerdt is a Lise Meitner fellow. We thank Romain Teyssier for his kindness in sharing simulation data with us. We acknowledge stimulating discussions with Yuval Birnboim, Nicolas Bouché and Oliver Czoske. The simulations were performed at the astro cluster at the Hebrew University of Jerusalem, at the National Energy Research Scientific Computing Centre, Lawrence Berkeley National Laboratory and at NASA Advanced Supercomputing at NASA Ames Research Center. Parts of the computational calculations were done at the Vienna Scientific Cluster under project number 70522. The authors would like to thank Jorge Sánchez Almeida and the Instituto de Astrofísica de Canarias for their hospitality, where parts of this work were carried out. This work was supported by FWF project number M 1590-N27.

## REFERENCES

- Agertz O. et al, 2007, MNRAS, 380, 963  
 Agertz O, Teyssier R, Moore B, 2009, MNRAS, 397L, 64  
 Agertz O, Teyssier R, Moore B, 2011, MNRAS, 410, 1391  
 Agertz O, Kravtsov A. V, Leitner S. N, Gnedin N. Y, 2013, ApJ, 770, 25  
 Basu-Zych A, Scharf C, 2004, ApJ, 615, 85  
 Birnboim Y, Dekel A, 2003, MNRAS, 345, 349  
 Bouché N. et al, 2010, ApJ, 718, 1001  
 Bouché N, Murphy M. T, Kacprzak G. G, Péroux C, Contini T, Martin C. L, Dessauges-Zavadsky M, 2013, Science, 341, 50  
 Cacciato M, Dekel A, Genel S, 2012, MNRAS, 421, 818  
 Ceverino D, Klypin A. A, 2009, ApJ, 695, 292  
 Ceverino D, Dekel A, Bournaud F, 2010, MNRAS, 404, 2151  
 Ceverino D, Dekel A, Mandelker N, Bournaud F, Burkert A, Genzel R, Primack J, 2012, MNRAS, 420, 3490  
 Ceverino D, Klypin A, Klimek E. S, Trujillo-Gomez S, Churchill C. W, Primack J, Dekel A, 2014, MNRAS, 442, 1545  
 Ceverino D, Dekel A, Tweed D, Primack J, 2015, MNRAS, 447, 3291  
 Ceverino-Rodriguez D, 2008, Ph.D. Thesis, New Mexico State University  
 Chapman S. C, Lewis G. F, Scott D, Richards E, Borys C, Steidel C. C, Adelberger K. L, Shapley A. E, ApJ, 548, 17  
 Cuesta A. J, Prada F, Klypin A, Moles M, 2008, MNRAS, 389, 385  
 Daddi E. et al, 2010, ApJ, 713, 686  
 Dalla Vecchia C, Schaye J, 2008, MNRAS, 387, 1431  
 Danovich M, Dekel A, Hahn O, Ceverino D, Primack J, 2015, MNRAS, 449, 2087  
 Dekel A, Birnboim Y, 2006, MNRAS, 368, 2  
 Dekel A. et al, 2009a, Nature, 457, 451  
 Dekel A, Sari R, Ceverino D, 2009b, ApJ, 703, 785  
 Dekel A, Zolotov A, Tweed D, Cacciato M, Ceverino D, Primack J. R, 2013, MNRAS, 435, 999  
 Dubois Y, Teyssier R, 2008, A&A, 477, 79  
 Fardal M. A, Katz N, Gardner J. P, Hernquist L, Weinberg D. H, Davé R, 2001, ApJ, 562, 605  
 Faucher-Giguere C. A, Kereš D, Dijkstra M, Hernquist L, Zaldarriaga M, 2010, ApJ, 725, 633  
 Ferland G. J, Korista K. T, Verner D. A, Ferguson J. W, Kingdon J. B, Verner E. M, 1998, PASP, 110, 761  
 Fumagalli M, Prochaska J. X, Kasen D, Dekel A, Ceverino D, Primack J. R, 2011, MNRAS, 418, 1796  
 Geach J. E. et al, 2005, MNRAS, 363, 1398  
 Geach J. E, Smail I, Chapman S. C, Alexander D. M, Blain A. W, Stott J. P, Ivison R, 2007, ApJ, 655, 9  
 Genel S, Dekel A, Cacciato M, 2012, MNRAS, 425, 788  
 Genzel R. et al, 2010, MNRAS, 407, 2091  
 Genzel R. et al, 2011, ApJ, 733, 101  
 Goerdt T, Dekel A, Sternberg A, Ceverino D, Teyssier R, Primack J. R, 2010, MNRAS, 407, 613  
 Goerdt T, Dekel A, Sternberg A, Gnat O, Ceverino D, 2012, MNRAS, 424, 2292  
 Goerdt T, Burkert A, Ceverino D, 2013, arXiv:1307.2102  
 Goerdt T, Ceverino D, Dekel A, Teyssier R, 2015, arXiv:1505.01486  
 Grevesse N, Sauval A. J, 1998, SSRv, 85, 161  
 Haardt F, Madau P, 1996, ApJ, 461, 20  
 House H, Dekel A, in preparation  
 Ibata R. A. et al, Nature, 2013, 493, 62  
 Katz N, Hernquist L, Weinberg D. H, 1992, ApJ, 399, 109  
 Kennicutt R. C, 1998, ApJ, 498, 541  
 Kereš D, Katz N, Weinberg D. H, Davé R, 2005, MNRAS, 363, 2  
 Kereš D, Katz N, Fardal M, Davé R, Weinberg D. 2009, MNRAS, 395, 160  
 Kravtsov A. V, Klypin A. A, Khokhlov A. M, 1997, ApJS, 111, 73  
 Kravtsov A. V, 2003, ApJ, 590, 1  
 Krumholz M, Burkert A, 2010, ApJ, 724, 895



- Mandelker N, Dekel A, Ceverino D, Tweed D, Moody C. E, Primack J, 2014, MNRAS, 443, 3675
- Miller G. E, Scalo J. M, 1979, ApJS, 41, 513
- Nelson D, Vogelsberger M, Genel S, Sijacki D, Kereš D, Springel V, Hernquist L, 2013, MNRAS, 429, 3353
- Nelson D, Genel S, Vogelsberger M, Springel V, Sijacki D, Torrey P, Hernquist L, 2015a, MNRAS, 448, 59
- Nelson D, Genel S, Pillepich A, Vogelsberger M, Springel V, Hernquist L, 2015b, arXiv:1503.02665
- Ocvirk P, Pichon C, Teyssier R, 2008, MNRAS, 390, 1326
- Prescott M. K. M, Momcheva I, Brammer G. B, Fynbo J. P. U, Møller P, 2015, ApJ, 802, 32
- Robertson B. E, Kravtsov A. V, 2008, ApJ, 680, 1083
- Rosdahl J, Blaizot J, 2012, MNRAS, 423, 344
- Scarlata C. et al, 2009, ApJ, 706, 1241
- Schaye J, Dalla Vecchia C, 2008, MNRAS, 383, 1210
- Springel V, Hernquist L, 2003, MNRAS, 339, 289
- Steidel C. C, Bogosavljevic M, Shapley A. E, Kollmeier J. A, Reddy N. A, Erb D. K, Pettini M, 2011, ApJ, 736, 160
- Teklu A, 2012, Bachelor Thesis, LM University Munich
- Teyssier R, 2002, A&A, 385, 337
- Truelove J. K, Klein R. I, McKee C. F, Holliman J. H, Howell L. H, Greenough J. A, 1997, ApJ, 489, 179
- van de Voort F, Schaye J, 2012, MNRAS, 423, 2991
- Wetzell A. R, Nagai D, 2014, arXiv:1412.0662
- Woosley S. E, Weaver T. A, 1995, ApJS, 101, 181
- Yepes G, Kates R, Khokhlov A, Klypin A, 1997, MNRAS, 284, 235